Investigating the fracture and deformation behaviour of pre-strained Grade 91 steel under small punch loading

S. C. Pandit
Faculty of Mechanical and Automotive Engineering Technology, Universiti Malaysia Pahang Al-Sultan Abdullah (UMPSA), 26600, Pekan, Pahang, Malaysia
sarthokchandrapandit@gmail.com

N. A. Alang*, J. Alias
Faculty of Mechanical and Automotive Engineering Technology, Universiti Malaysia Pahang Al-Sultan Abdullah (UMPSA), 26600, Pekan, Pahang, Malaysia
Center for Advanced Industrial Technology, Universiti Malaysia Pahang Al-Sultan Abdullah (UMPSA), 26600, Pekan, Pahang, Malaysia
azuan@umpsa.edu.my, juliawati@umpsa.edu.my

M. F. Hassan, A. H. Ahmad, M. S. Shaari
Faculty of Mechanical and Automotive Engineering Technology, Universiti Malaysia Pahang Al-Sultan Abdullah (UMPSA), 26600, Pekan, Pahang, Malaysia
firdaus@umpsa.edu.my, asnul@umpsa.edu.my, shamil@umpsa.edu.my

L. Zhao
School of Materials Science and Engineering, Tianjin University, Tianjin, 300350, People's Republic of China
zhaolei85@tju.edu.cn

ABSTRACT. Various failure modes induce localized internal damage and stress concentration sites in power plant components, causing additional plasticity that degrades material strength. Effect on such localized plasticity on components durability cannot be accurately evaluated using conventional mechanical tests which require large specimens. This study investigates the effect of plasticity on the deformation and fracture behaviour of Grade 91 steel using small punch testing (SPT). Initially, plasticity was introduced by mechanically pre-straining the material to 4%, 8%, and 12% strain levels. The deformation and fracture behaviour of the pre-strained specimens were then assessed under small punch loading. Pre-straining significantly influences the load–displacement response, producing a clear increase in yield load, while the

Citation: Pandit, S. C., Alang, N. A., Alias, J., Hassan, M. F., Ahmad, A. H., Shaari, M. S., Zhao, L., Investigating the fracture and deformation behaviour of pre-strained Grade 91 steel under small punch loading, Fracture and Structural Integrity, 77 (2026) 340-361.

Received: 20.02.2026
Accepted: 21.05.2026
Published: 28.05.2026
Issue: 07.2026

maximum load and corresponding displacement decrease progressively with increasing pre-strain. Moreover, fracture occurs at lower displacement values at higher pre-strain levels. At the macroscopic scale, fracture exhibits mixed ductile–brittle characteristics with limited necking. Microscopic observations further confirm a pronounced reduction in ductility with increasing pre-strain. Furthermore, numerical simulations accurately predict the onset and location of fracture as well as the stress distribution in SPT samples, validating the modelling approach for pre-strained materials. Overall, this study supports improved assessment of structural integrity in components subjected to long-term plastic deformation.

KEYWORDS. Deformation, Fracture, Grade 91 Steel, Pre-straining, Small Punch.

INTRODUCTION

In power generation plants, components such as superheated pipes and headers are subjected to static and cyclic loading conditions at elevated temperatures. The strength of these components is designed to sustain prolonged operation without premature failure. However, after several years of service, localized damage can develop in the material due to various mechanisms, including creep, fatigue, corrosion, and thermal stress. Such mechanisms frequently induce defects such as cracks, pits, or micro-voids in the components. Jin et al. [1] found that plastic strain may accumulate near these defects, and the effect is more pronounced in steels, including martensitic-ferritic steels such as Grade 91 (9Cr-1Mo). For instance, researchers [2][3] found that Grade 91 steel is prone to low-cycle fatigue, which leads to microstructural changes such as dislocation annihilation and martensite lath migration, thereby contributing to reduced yield strength and accelerated crack initiation. Moreover, fatigue deformation in Grade 91 weld zones weakens tensile properties, as strain cycling induces plastic strain accumulation, consequently reducing fatigue life due to the early development of micro-cracking in inter-critical heat-affected zones. Similarly, Grade 91 steel can be vulnerable to room-temperature corrosion in environments containing moisture, dissolved salts, or oxygen. Pitting corrosion can lead to localized material damage, weakening the steel surface properties as well as the bulk material strength. A Study by Abebe et al. [4] found that pitting corrosion can facilitate hydrogen diffusion, enhancing embrittlement and reducing ductility. Pitting acts as a strong local stress concentrator, which accumulates local plastic strain in the surrounding region. Hydrogen embrittlement (HE) is another prominent degradation mechanism for Grade 91 steel, particularly when it is exposed to hydrogen or hydrogen-generating environments. HE causes a loss of ductility, as hydrogen atoms diffuse into the steel matrix, accumulating around defects and grain boundaries, leading to brittle fracture. Junak [5] reported that HE is associated with intergranular fracture and can significantly reduce the load-bearing capacity of the components. In addition, some materials operating under extreme conditions, such as Grade 91 steel, exhibit plastic strain development even in the absence of observable cracks or voids. Plastic strain tends to accumulate at austenite grain boundaries and martensitic lath boundaries well before any visible voids or cracks appear [6]. Since this steel is widely used under extreme temperature and pressure conditions, the development of plastic strain in this material is inevitable. This localized plasticity can significantly affect the deformation and fracture behaviour of Grade 91 steel [7]. Assessing the deformation and fracture behaviour of components with plasticity-induced damage is essential to better understand its effects on mechanical properties and overall material performance.

Conventional mechanical testing, such as uniaxial tensile or compression tests, focuses only on the bulk material properties and often overlooks the effect of localized deterioration caused by the plastic deformation or damage present in a component. In this context, the SPT can be a viable solution due to its capability to determine mechanical properties using a small-sized specimen that may be extracted from the damage-affected area. Small punch test allows specimen extraction using scooping method at several points of a component even during the running operation. This is not possible in conventional testing, as extracting a large specimen will stop the operation of the component. Another key advantage of SPT is cost-effectiveness. Small punch method can predict several mechanical properties using less complex equipment. Therefore, it offers a more affordable alternative for material characterization. Recently, researchers [8] are inquiring and improving this method for various materials, mainly steels and alloys, nuclear and irradiated materials. In addition, plasticity induced materials are being investigated under small punch loading. In early researches, SPT is assumes to has a baseline material condition, where it is considered that the specimens are isotropic, exhibit linear strain-hardening behaviour, or have

no prior hardening [9]. To simulate the effect of plasticity, Cuesta and Alegre [10] applied pre-strain on aluminum alloy sheets and later evaluated under a small punch load. They found that new expressions were necessary to predict yield strength accurately, as pre-strained materials exhibited altered SPT responses. The authors [10] concluded that each pre-strained condition requires its own set of calibration constants or an updated model that incorporates hardening behavior, anisotropy, and strain history. It is also found that pre-straining can change the entire shape of the SPT load-displacement curve by increasing the material's yield load and modifying the elastic-plastic transition. In another study, Shu et al. [11] investigated 310S stainless steel and observed that both the yield strength and maximum punch load increased proportionally with pre-strain level. However, the location and nature of inflection points on the curve also shifted, indicating a different deformation mechanism. These changes reflect the effects of strain hardening, which increases resistance to plastic flow and alters stress distribution under the punch. The study emphasized that interpreting characteristic SPT parameters without considering pre-strain can lead to inaccurate in ultimate tensile strength (UTS) or yield strength predictions. Similarly, Peng et al. [12] focused on the mechanical characterization of pre-strained 316L stainless steel using SPT. Pre-straining increases dislocation density and causes strain hardening, leading to an enhanced yield load. However, the increase in this load due to pre-straining does not linearly correlate with the actual increase in yield strength. Even though the maximum load was reported to remain nearly constant, the fracture energy decreased with increasing pre-strain. To better understand the phenomenon, finite element modeling was performed. Calaf-Chica et al. [13] carried out finite element simulations of SPT on hypothetical materials. They introduced kinematic hardening models into their simulations to accurately reproduce the effects of prior plastic straining. Yield strength and UTS of the material were estimated and compared with the experimental data, obtained from uniaxial tensile test under the same pre-straining conditions. Their study found that pre-strained diminishes isotropic material characteristics. Furthermore, pre-straining can distort the elastic–plastic transition, leading to errors when using standard empirical correlations are employed. Plastic pre-straining can induce anisotropy and strain hardening, which causes complex material deformation responses and fracture behavior [14].

Although SPT has been widely applied to various steels, especially austenitic stainless steels such as pre-strained 316L stainless steel and 310S stainless steel, there exists very limited literature specifically addressing the deformation and fracture behaviour of pre-strained Grade 91 steel. Although all three grades serve elevated-temperature power plant and petrochemical applications, the routes by which they accommodate plasticity, accumulate damage, and fracture diverge in ways that critically affect life assessment and failure prediction. Grade 91 steel contents $M_{23}C_6$-type carbides that form at the boundaries of prior austenite grains (PAGs), packets, blocks, and martensitic laths, while MX carbonitrides precipitate within the martensitic matrix. Due to this hierarchical microstructure, abundant dislocations are present at grain boundaries. This produce pronounced back stress, high initial yield strength, and strong resistance to plastic strain accumulation during loading [15]. On the other hand, austenitic stainless steels (316L & 310S stainless steel) possess a uniform equiaxed FCC austenitic microstructure whose deformation is governed by stacking fault energy (SFE). This SFE-governed transition can activate a secondary deformation mechanism, such as twinning to sustain plasticity and delay necking in a way that Grade 91 cannot [16]. Moreover, creep deformation in Grade 91 is governed by its hierarchical lath martensitic architecture [17]. At elevated-temperature, creep in P91 progressively destroys the lath sub-structure through lath widening, recrystallisation, dislocation density reduction, and $M_{23}C_6$ coarsening, culminating in creep cavitation. In contrast, in austenitic steels like 316L and 310S, creep deformation is primarily controlled by dislocation climb and glide. Since austenitic steels have an FCC structure with relatively wide dislocation spacing and no lath boundary confinement, dislocations can climb over obstacles (like precipitates or solute atoms) more freely at elevated temperatures. The creep rate is therefore governed by how fast dislocations can climb, which depends on vacancy diffusion [18]. Since the deformation and fracture behaviour of Grade 91 steel is governed by its unique hierarchical lath martensitic microstructure, coupled dislocation–precipitate interactions, and multi-scale boundary strengthening , all of which are absent in austenitic steels, it is reasonable to expect that the small punch test response of plastically pre-strained Grade 91 steel will be distinctly different from that of austenitic grades. Hence, this study aims to fill this gap by investigating the effectiveness of SPT in accurately predicting the deformation and fracture behaviour of pre-strained Grade 91 steel.

The mechanical response obtained from SPT is governed by highly complex deformation mechanisms, along with evolving contact interactions between the punch, specimen, and dies. Finite element modelling (FEM) enables simulation of detailed stress and strain distributions within the material, which are difficult to capture through experimental methods alone. Cheng et al. [19] demonstrated that incorporating FEM-based models into SPT curve analysis reduces scatter in yield strength predictions, particularly within the elastic and plastic regimes. In addition, Calaf-Chica et al. [13] conducted a three-dimensional finite element study to investigate the effects of pre-straining and the Bauschinger effect on the estimation of yield strength and ultimate tensile strength. The results indicated that in the absence of isotropy induced by pre-straining, SPT provides an average value of the principal yield strength components of the yield surface. Furthermore, Shu et al. [11] performed a two-dimensional simulation of SPT on 310S stainless steel incorporating pre-strain effects, with the numerical

model validated against experimental results. Despite the increasing use of numerical methods in SPT, only a limited number of studies have considered the influence of initial stress or pre-straining in the Grade 91 steel.
Based on available literature, there are very few experimental works and numerical studies on Grade 91 steel that explicitly consider the influence of pre-straining. Therefore, the development of a comprehensive three-dimensional FEM model for SPT of Grade 91 steel, incorporating pre-strain effects, is necessary. For this reason, the present study integrates both experimental and finite element (FE) modelling approaches. Two material conditions, namely as-received and pre-strained materials, are considered and are subjected to small punch loading. Additionally, FE modelling, which incorporates different material hardening data, is employed to simulate the effects of plasticity on material deformation and fracture behaviour. The experimental procedure and modeling techniques used in the present work are systematically reported.

MATERIALS AND METHODS

Cylindrical rods with a diameter of 10 mm and a length of 160 mm were extracted from as-received commercial Grade 91 steel pipes using wire electrical discharge machining (EDM). The rods were extracted in the rolling direction of the pipe. They were carefully machined so that the geometry and the dimensions were accordance to the standard test methods for tension testing of metallic materials ASTM E8 standard [20]. The specimens were prepared for uniaxial tensile and plastic pre-straining tests. Both uniaxial tensile and plastic pre-straining tests were performed using Universal Testing Machine (UTM). A total of nine (9) specimens were prepared for the tests with three (3) specimens used for standard uniaxial tensile testing and the remaining specimens used for pre-straining tests. Prior to the test, a tensile test rig was installed on the machine. After the specimens were properly gripped, an extensometer was attached to the gauge area of the specimen to accurately measure the displacement and strain during the test. A pre-load of 50 N was applied during the test to ensure that there was no initial slip between the specimen and the grips, which could affect the accuracy of the measurements. The testing machine was set to run at a constant displacement speed of 0.375 mm/min during the tests. For standard uniaxial tensile tests, the specimens were strained up to their fracture point to determine the mechanical properties of the material. These properties included yield strength, modulus of elasticity, ultimate tensile strength, ductility and plastic hardening. Subsequently, the properties obtained from the tests were used as input data for the material model in finite element simulations. The remaining six specimens were subjected to predetermined pre-strain levels of 4%, 8%, and 12%, with two specimens tested at each level. Tab. 1 summarizes the test program, while Fig. 1 depicts the uniaxial tensile and pre-straining experimental setups.

Specimen ID	Test End Condition	No. of Specimens
Uni-ST	Until Fracture	3
Uni-PS-4%	4% Strained	2
Uni-PS-8%	8% Strained	2
Uni-PS-12%	12% Strained	2

Table 1: Test program of standard uniaxial tensile and pre-straining tests

The pre-strained specimens were carefully sliced at the mid-section using a high-precision sectioning machine (see Fig. 1). A total of eight (8) specimens were prepared as detailed in Tab. 2. The small punch test was performed at room temperature following the standard test method for small punch testing of metallic materials ASTM 3205 standard [21]. The pre-load of 50 N and displacement rate of 0.375 mm/min were employed as similar to the uniaxial tensile test to avoid any discrepancy due to loading rate effects. The test was stopped when the specimen showed signs of fracture, indicated by an approximate 20% drop in maximum force according to the standard. Punch displacement was recorded using an extensometer and subsequently compared with displacement data obtained from the Universal Testing Machine (UTM). Each specimen condition was tested twice to confirm repeatability of the test results. The small punch test setup is shown in Fig. 2.
The yield load, P_y, estimated from the load-displacement curves can be correlated with the material yield strength. The yield load was determined by identifying the point where the material deformation transitions from the elastic to the plastic region. In the present study, four different methods for determining the yield loads were used, namely Mao, CEN, t/10 and t/100 [22] [23]. Fig. 3 illustrates the definition of the yield load based on the four methods mentioned above. Furthermore, the maximum load was determined at the point that marks the highest force reached during the test.

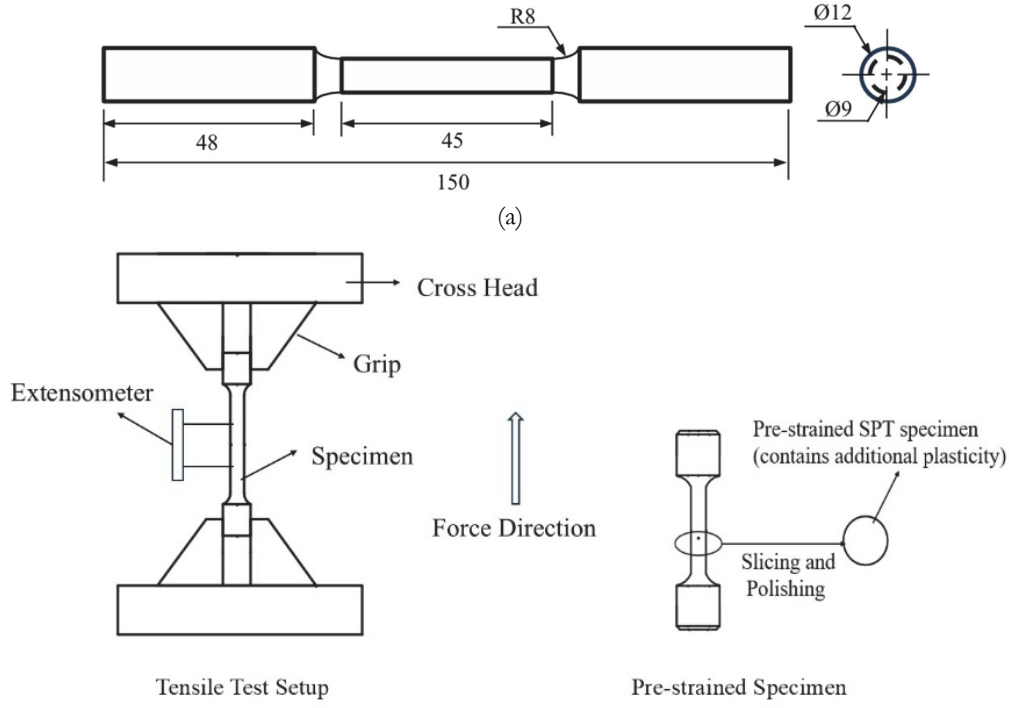

Figure 1: (a) Dimension of uniaxial tensile test specimens (b) Uniaxial tensile and pre-straining test setup.

Specimen ID	Specimen Condition
SP_AR_01	As received
SP_AR_02	
SP_4%_01	4% Pre-strained
SP_4%_02	
SP_8%_01	8% Pre-strained
SP_8%_02	
SP_12%_01	12% Pre-strained
SP_12%_02	

Table 2: Small punch test matrix.

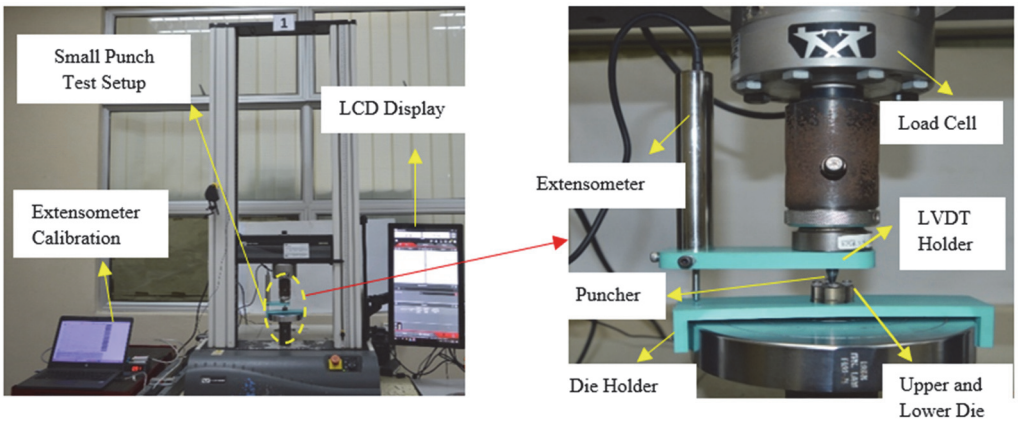

Figure 2: Small punch test setup.

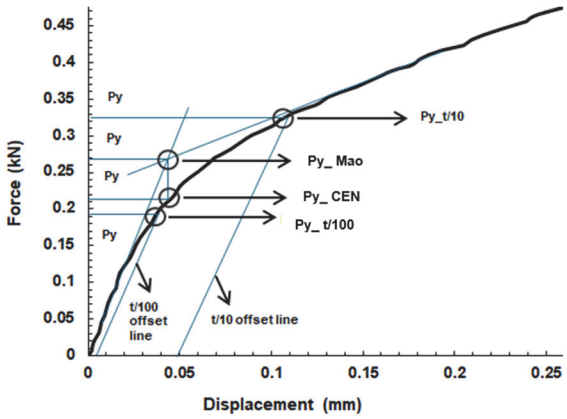

Figure 3: Yield load estimation based on different methods.

The yield strength can then be estimated using Eqn. (1) [23].

$$\sigma_{ys} = \alpha_1 \left(\frac{P_y}{t^2} \right) + \alpha_2 \tag{1}$$

where, σ_{ys} is the yield strength, t is the specimen thickness and α_1, α_2 are the correlation constants. On the other hand, the ultimate tensile strength of the material can be estimated using the following empirical relationship [19]:

$$\sigma_{uts} = \beta_1 \left(\frac{P_{max}}{t^2} \right) + \beta_2 \tag{2}$$

where, σ_{uts} is the ultimate tensile strength, β_1 and β_2 are the correlation constants.

The value of α_1, α_2, β_1 and β_2 are determined by fitting empirical correlations between normalized SPT loads (F / t^2) and tensile properties using regression analysis. The slope gives α_1 and β_1 values, and the intercept gives α_2 or β_2. Moreover, their value varies depending on the material and specimen geometry. For instance, they are sensitive to the specimen thickness as thinner or thicker specimens alter the stress and strain distributions [24]. After the small punch tests, the fracture surface of the specimen was examined using scanning electron microscopy (SEM). The fractured specimen was mounted onto a sample holder properly before being analyzed under the SEM. A sliced specimen was also examined to identify the deformation behaviour of the material. For this reason, the specimen was half-sliced and mounted into the holder using the cold-mount technique. Fig. 4 shows the sample preparation process for the SEM examination.

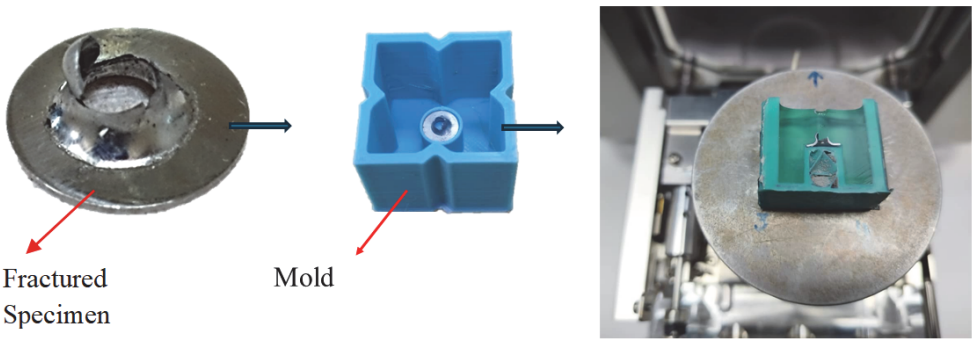

Figure 4: Sample preparation for SEM examination.

During the small punch test, the displacement of the specimen was measured using an extensometer. As fracture is an unstable and rapid process, therefore, the measurement of the total displacement may be inaccurate, with the possibility of missing the full deformation profile. Therefore, optical techniques using a profile projector were employed to measure the total displacement. During the measurement, the specimen fracture edge was positioned as shown in Fig. 5 to obtain a clear

and sharp projected image. Using the profile projector's digital readout and screen overlay grid, the displacement at fracture, δ_f was measured. For each specimen, the δ_f value was measured three times, and the average value was reported to ensure measurement consistency.

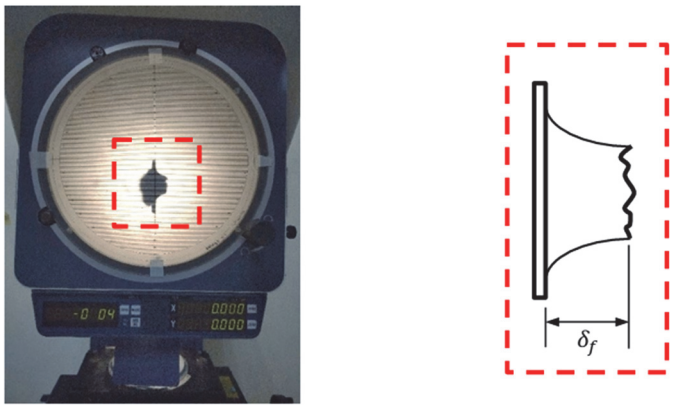

(a) (b)

Figure 5: Displacement at fracture: (a) Measurement setup using profile projector and (b) Length of measurement.

The commercial finite element (FE) software Abaqus v2024 was used to simulate the material deformation response and fracture behaviour of Grade 91 steel subjected to a punch load under the influence of plastic pre-straining. The overall FE procedures were divided into three steps: pre-processing, solving and post-processing. A three-dimensional (3D) FE model was created to represent the physical setup of the small punch test. Due to the geometry symmetry, a quarter model instead of a full model was developed to ensure computational efficiency. Next, the specimen was assigned with elastic-plastic material properties with isotropic hardening using the 'Material' module option in the Abaqus software. This material data was obtained from the uniaxial tensile test as discussed earlier. Additionally, an isotropic homogeneous material model was employed. The elastic properties values assigned to the specimen include the modulus of elasticity, E = 210 GPa and the poisson ratio, υ = 0.3. Elastic material behaviour obeys Hooke's Law, according to:

$$\sigma = E\varepsilon \tag{3}$$

where, σ is the stress, and ε is the elastic strain. On the other hand, the plastic deformation behaviour (plastic hardening) follows the power-law relationship, expressed as follows:

$$\sigma = K \cdot \epsilon^{n} \tag{4}$$

where, ϵ is the true plastic strain, K is the strain coefficient and n is the strain hardening constant. For the pre-strained specimen, the true plastic stress-strain data were extracted starting from 4%, 8% and 12% strain, as illustrated in Fig. 6. For example, point '*a*', '*b*' and '*c*' are the starting point of the plastic data for the 4%, 8%, and 12% pre-strained specimens, respectively.

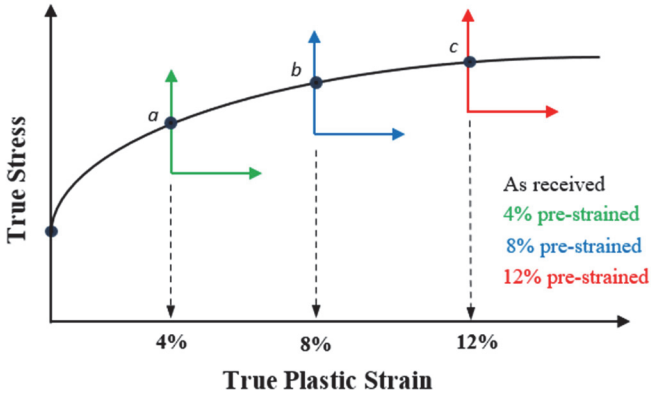

Figure 6: Representation of true plastic stress-strain data extraction.

In the present study, no damage model was incorporated into the FEM simulation. The analysis focused on reproducing the elastic-plastic load-displacement response of the SPT specimen. Failure initiation was implicitly defined by the attainment of maximum punch load, P_{max}, consistent with established SPT correlations for yield strength and UTS estimation [13]. The interaction properties were defined at all the contact surfaces between the punch-specimen and die-specimen. Surface-to-surface contact with finite sliding model was chosen for the sliding formulation. The friction coefficient value of μ = 0.3 was adopted in the contact definition [25]. This value was selected as it provides results that closely match the experimental force-displacement curve. Furthermore, appropriate boundary conditions were defined to replicate the actual three-dimensional small punch test setup. The punch was constrained in all directions except the y-direction, where a prescribed downward displacement of 3 mm was applied to simulate the experimental loading condition. The upper and lower dies were fully constrained to prevent specimen movement. Owing to the quarter-model geometry, symmetry boundary conditions were applied: the YZ plane was restricted in the x-direction and y- and z-rotations, while the XY plane was constrained in the z-direction and x- and y-rotations. In present study, 8-node linear brick elements with reduced integration scheme (C3D8R) were employed. A mesh sensitivity analysis was performed prior to the simulation to identify the optimal mesh size for computational efficiency. During mesh sensitivity analysis, identical boundary conditions and loading were applied across all variations for model consistency. The maximum force and maximum von-Mises stress was plotted against the number of elements to identify the mesh independence point. An illustration of the boundary conditions and finite element meshes applied to the model is shown in Fig. 7.

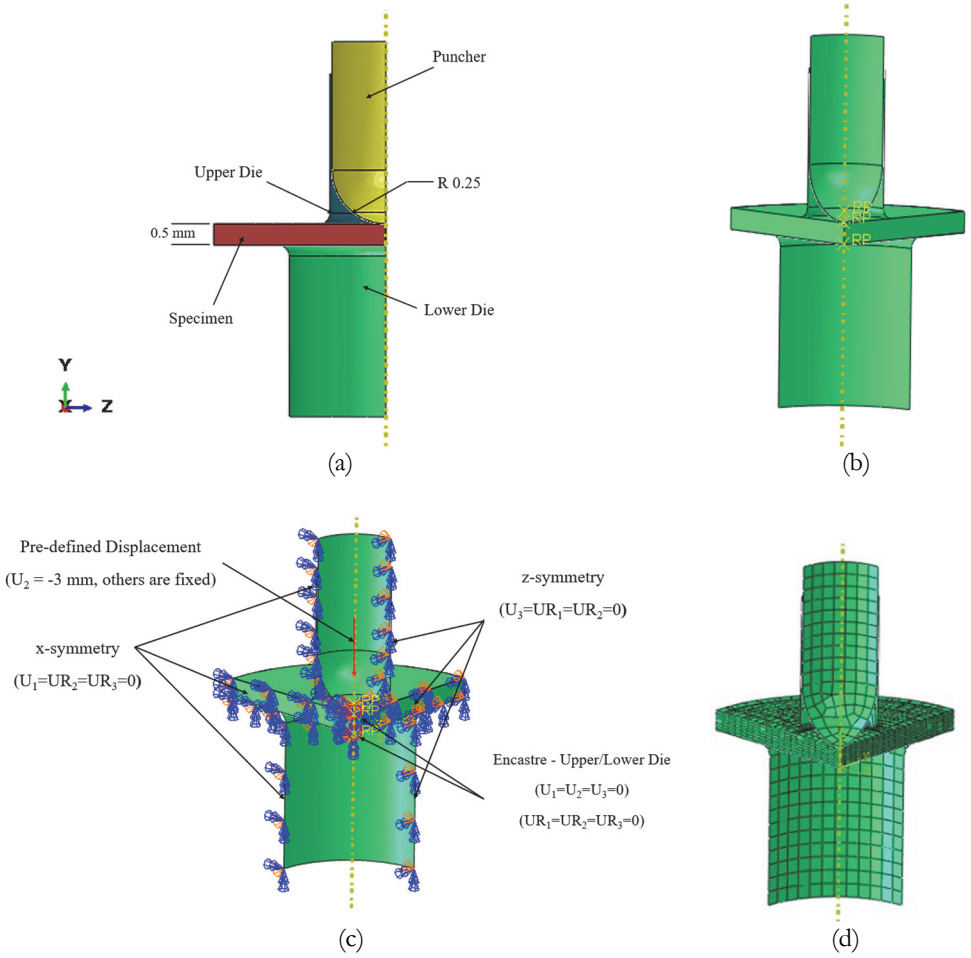

Figure 7: (a) Small punch FE model, (b) Reference point, (c) Detailed boundary conditions and (d) Mesh.

RESULTS AND DISCUSSION

Fig. 8 shows the stress-strain curve of as-received Grade 91 material. The true stress-strain curve is also plotted in the same figure. From the curves, it is observed that as-received material exhibits ductile behaviour, with approximately 40% ductility. The material exhibits elastic-plastic deformations with clear strain-hardening up to ultimate tensile

strength (UTS). Beyond this point, stress gradually decreases and leads to necking and eventual fracture. The Young's modulus of Grade 91 steel is found to be 210 GPa. Meanwhile, using the 0.2% offset method, the yield strength is found to be 353 MPa. The ultimate tensile strength is observed to be 601.54 MPa. These values were later used as input data for finite element modelling. Fig. 9 shows the engineering stress-strain curve obtained from full tensile test and pre-straining of Grade 91 steel at different strain levels. It should be noted that the curves for the pre-strained specimen consistently follow the as-received curve, indicating good repeatability of the test. The corresponding yield strength for 4%, 8%, and 12% pre-strained specimens are 460 MPa, 533 MPa, and 595 MPa, respectively. These values are used as an initial stress value in plastic material model of pre-strained material during finite element modelling. The modulus of elasticity for all pre-straining specimens was found to be constant at 210 GPa.

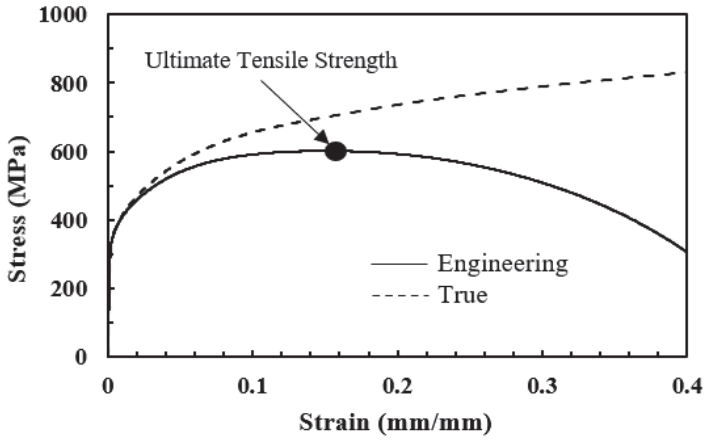

Figure 8: Engineering and true stress-strain curve of as received material.

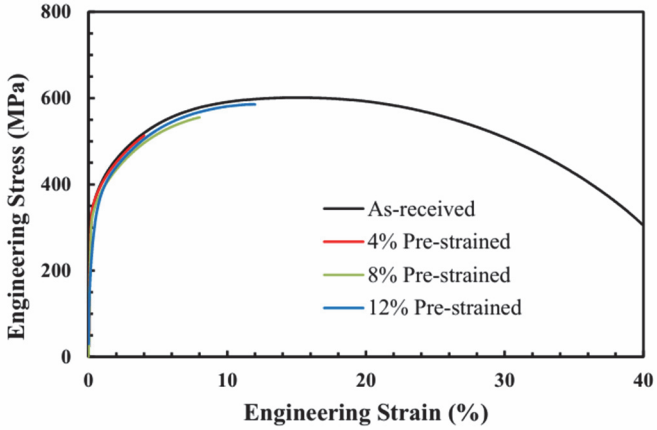

Figure 9: Engineering stress-strain curve at different pre-straining levels.

For computational efficiency, mesh sensitivity analysis was performed prior to the main simulation works. Based on the analysis, it was observed that after 7595 elements, the value of both maximum load and von-Mises stress begins to stabilize, indicating that any further refinement on the mesh size would not affect the FE results. Based on this finding, the number of elements chosen for the entire simulation was 7595, to ensure both prediction accuracy and computational efficiency.
Fig. 11 presents the load–displacement responses obtained from both finite element simulations and experiments for the as-received and pre-strained (4%, 8%, and 12%) Grade 91 steel specimens. The curves exhibit five typical deformation stages, including elastic deformation, plastic bending, membrane stretching, plastic instability, and fracture. The elastic region extends to a punch displacement of approximately 0.15 mm and shows a linear load–displacement response for all conditions. Yield loads increase systematically with increasing pre-strain. Based on the CEN method, the experimental yield load increases from 180 N in the as-received condition to 280 N, 300 N, and 330 N for 4%, 8%, and 12% pre-strain, respectively (see Tab. 3). Although quantitative differences are observed among the yield load determination methods, all approaches consistently indicate a substantial increase in yield load with increasing pre-strain. The results are consistent with the uniaxial tensile test data (see Fig. 9), which also show the same trend. This confirming that the small punch test can effectively capture the trend of yield strength variation resulting from prior plastic deformation.

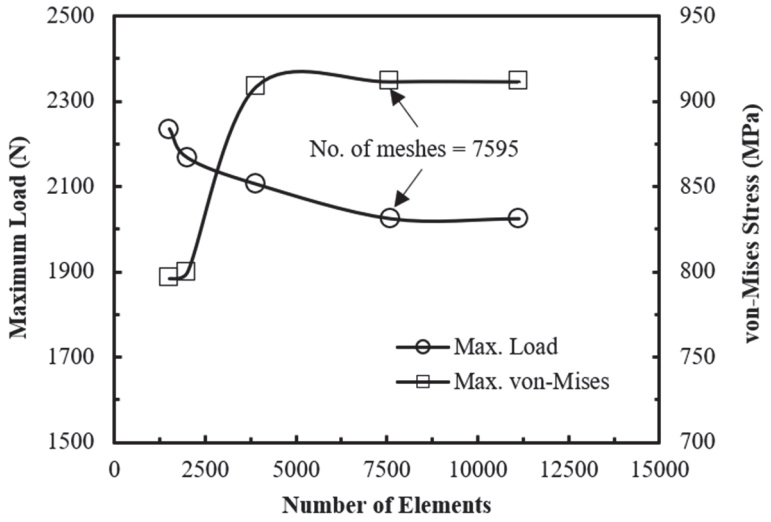

Figure 10: Mesh Sensitivity Analysis.

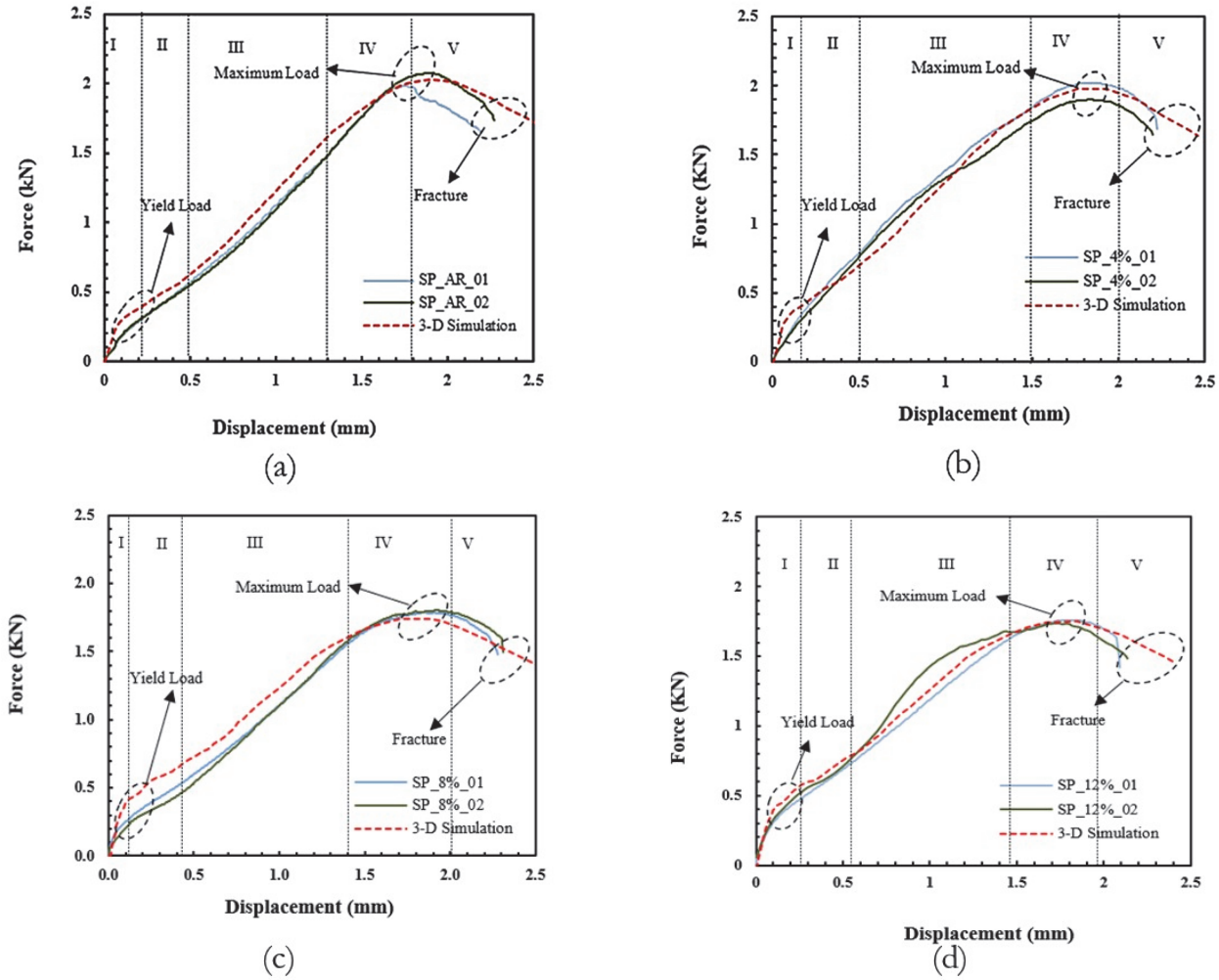

Figure 11: Load-displacement curve of (a) As-received specimen, (b) 4% pre-strained specimen, (c) 8% pre-strained specimen, (d) 12% pre-strained specimen.

In the later deformation stages, namely plastic bending (0.15–0.5 mm punch displacement) and membrane stretching (0.5–1.4 mm punch displacement), all curves exhibit a similar increasing load trend. However, the specimens with 12% pre-strain

display a noticeably stiffer response compared to the other conditions. This behavior is likely associated with the development of material anisotropy under significant work hardening [14,26]. Beyond a punch displacement of approximately 1.4 mm, the curves begin to deviate, marking the onset of the plastic instability regime. The maximum load for the as-received material is approximately 2100 N (see Tab. 4). With increasing pre-strain, the maximum load gradually decreases (see Tab. 4 and Fig. 13), reaching about 1780 N at 12% pre-strain. The observed behavior arises from the competing effects of pre-straining. Pre-straining increases the dislocation density, which raises the flow stress through dislocation strengthening. In simple terms, more dislocations make further plastic deformation harder, so the material appears stronger initially. However, the high initial dislocation density reduces the material's capacity for further work hardening during subsequent loading. Since UTS depends on sustained strain hardening, this promotes earlier necking, leading to a reduction in strength. Moreover, the presence of stable MX and $M_{23}C_6$ precipitates in Grade 91 steel promotes saturation of strengthening mechanisms, thereby limiting further strengthening [27]. Consequently, the reduction in strength due to early necking outweighs the marginal increase from work hardening, resulting in a net decrease in UTS.

Pre-strain level (%)	CEN			Mao			t/10			t/100		
	Yield Load, P_y (N)											
	Exp.	Sim.	Error (%)	Exp.	Sim.	Error (%)	Exp.	Sim.	Error (%)	Exp.	Sim.	Error (%)
0	180	200	11.11	200	210	5	230	290	26	150	160	6.67
4	280	290	3.57	290	300	3.5	290	370	27	280	270	3.57
8	300	310	3.33	300	330	10	310	380	22	290	290	0
12	330	350	6.06	370	360	2.7	350	400	14	310	300	3.23

Table 3: Yield load estimation for different levels of pre-strained.

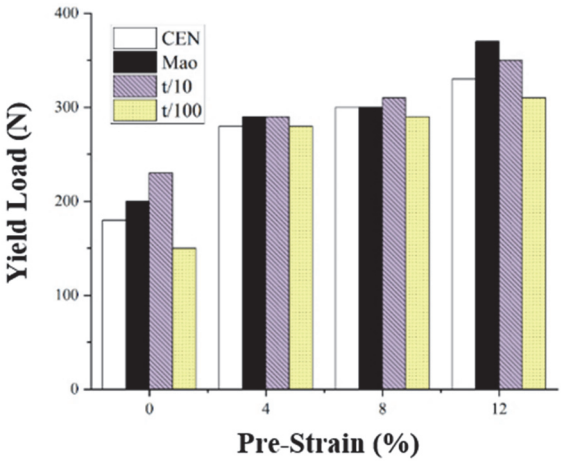

Figure 12: Yield load across different pre-strain levels.

Pre-strain level (%)	Maximum load by SPT (N)	Maximum load by FE (N)	Error (%)
0	2100	2030	3.34
4	1960	1970	0.50
8	1850	1740	5.94
12	1780	1750	1.68

Table 4: Maximum load across different pre-strained levels.

As summarized in Tab. 5, the corresponding displacement values at maximum load show only minor fluctuations under the influence of pre-strain levels. Quantitatively, the values are 1.85 mm, 1.77 mm, 1.88 mm, and 1.79 mm for 0%, 4%, 8%, and 12% pre-strain, respectively. Despite the absence of a clear overall trend, a comparison between the as-received and 12% pre-strained conditions indicates that the pre-strained material reaches its maximum load at a slightly lower displacement. Measurements obtained from the load-displacement curves indicate that the displacement at fracture decreases progressively with increasing pre-strain, reducing from 2.25 mm for the as-received condition to 2.13 mm for the 12% pre-strained specimen. This reduction reflects a loss of ductility associated with pre-straining, as prior plastic deformation limits the material's remaining capacity for further plastic flow [28]. Displacement at fracture measured using a profile projector follows the same trend, decreasing from 2.40 mm to 2.19 mm for the 0% and 12% pre-strained specimens, respectively. Later, it will show that increasing in pre-strain promotes a transition from ductile dimpled morphology to brittle, flat facets.

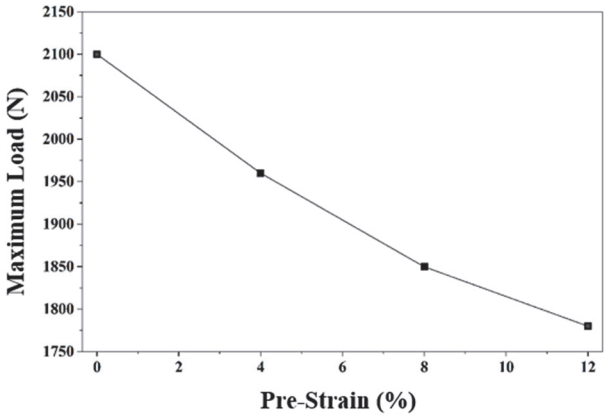

Figure 13: Maximum load across different pre-strain levels.

Different Types of Displacement	Displacement (mm)			
	0% Pre-strained	4% Pre-strained	8% Pre-strained	12% Pre-strained
Displacement at Fracture (LVDT)	2.25	2.22	2.21	2.13
Displacement at Fracture (Profile Projector)	2.40	2.38	2.31	2.19
Displacement at Max. Load	1.85	1.77	1.88	1.79

Table 5: Influence of pre-straining on displacement.

Based on the FE simulation results, it reproduce the five typical deformation regions observed in the small punch test, indicating that the modelling framework adequately captures the overall deformation behaviour of the pre-strained material (see Fig. 10). Minor discrepancies between the simulated and experimental curves are evident, particularly in the elastic and plastic bending regimes, where the FE model slightly overpredicts the load. These differences are attributed to an overestimation of strain hardening in the constitutive model, especially near the onset of tensile instability [29]. Quantitative comparison of yield load predictions as tabulated in Tab. 3 indicates that the Mao and t/100 methods provide consistently good agreement with experimental data across all pre-strain levels, with errors generally below 10%. The CEN method shows moderate accuracy, while the t/10 approach consistently overpredicts the yield load and exhibits the largest errors (see Fig. 14).

The FE-predicted maximum loads also show good agreement with experimental SPT results, with deviations remaining below 10% for all pre-strain conditions. The best agreement is observed at 4% pre-strain, while the largest deviation occurs at 8% pre-strain, likely reflecting uncertainties in the strain hardening input parameters. At the fracture stage, the FE model overpredicts the load-bearing capacity due to the absence of damage and fracture criteria, resulting in a gradual post-peak load reduction rather than the abrupt drop observed experimentally [30]. Despite this limitation, the FE simulations accurately capture the global load–displacement response across all deformation regimes, supporting the applicability of the modelling approach for small punch testing of pre-strained Grade 91 steel.

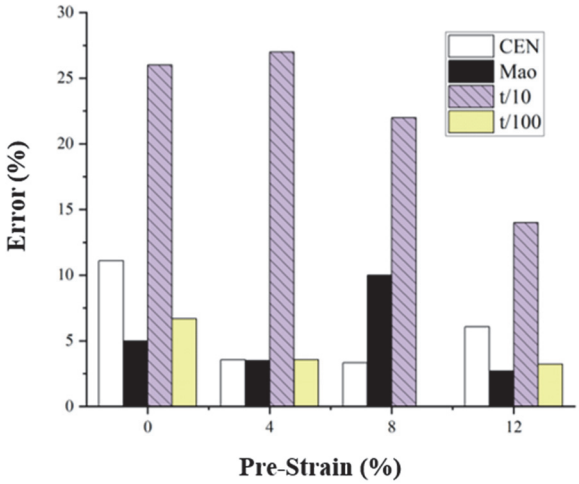

Figure 14: Error of yield load prediction across different pre-strain levels.

Figs. 15 and 16 show the FE von-Mises and equivalent plastic strain (PEEQ) contours showed the stress and strain distribution during small punch test. Although the overall spatial distributions of stress and strain are similar across all cases, their magnitudes and localization behavior differ, particularly with increasing pre-strain. In the elastic regime, stress is highly localized beneath the punch contact, where the maximum von-Mises stress occurs due to concentrated loading. As expected, no plastic strain develops at this stage. With increasing punch displacement, the specimen transitions into the plastic bending regime, where the stress field extends toward the bottom surface. The maximum stress at the bottom surface is consistent with classical bending theory, where tensile stresses are highest at the outer fiber. The initiation of non-zero PEEQ in this region indicates the onset of plastic yielding, marking the transition from elastic to elastoplastic behavior. with bending-induced curvature deformation visible. As the punch progresses, the specimen deformation enters to a membrane stretching zone. At this stage, the von-Mises stress increases proportionally to the punch displacement and spreads radially outward. Meanwhile, the plastic strain distribution is notably more extensive and maintains its pattern, indicating a dominant stretching behavior. Moreover, localized thinning (reduction of thickness) begins to develop, especially in the area between the specimen's center and contact edges between the punch and specimen. In the tensile instability zone, deformation becomes highly localized. The von-Mises stress distribution extends over a wider area, forming a 'cap' shape. The maximum stress occurs at the point offset from the specimen's center. The plastic strain becomes intensely concentrated at almost the same location as the highest von-Mises stress value. However, PEEQ contours show earlier strain localization in the 12% pre-strained specimen compared to as-received specimen. At this stage, the significant thinning and a sign of necking are observed. The thickness reduction in 0% pre-strained specimen was recorded to be 77%, while in 12% pre-strained specimen, the specimen reduction is almost 85% at the thinnest point. This trend is consistent with the one observed during macroscopic observations (see Figs. 17-20). Thickness reduction is more pronounced when pre-straining increased from 0% to 12%. From macroscopic observation, it is also noticeable that thinning occurred along with limited necking, whereas the FE contours predict more pronounced necking. This discrepancy is likely associated with the assumed friction conditions at the punch–specimen interface. In reality, the friction condition at the punch–specimen interface may evolve with contact pressure and surface conditions. Higher friction can restrict material flow, increasing stress triaxiality and promoting earlier strain localization [31,32]. Therefore, the present model may overestimate constraint effects, leading to exaggerated necking behavior. Hence, it is recommended to incorporate more realistic friction formulation, such as pressure dependent friction coefficient. At the final stage of deformation, the von-Mises stress value remains elevated along with a drop in maximum load. Overall, the FE contour analysis demonstrates that that pre-straining significantly influences localization behavior. The pre-strained specimen exhibits earlier onset of PEEQ localization and increased thickness reduction. For comparison, the von-Mises stress and PEEQ contours of the as-received and 12% pre-strained specimens are presented in Fig. 15 and 16, representing the lower and upper bounds of the pre-strain levels, respectively.

Figs. 17 to 20 show the macro-images of the fractured specimens under different conditions of as-received, 4%, 8% and 12% pre-strained. It is clearly observed that the fractures occur at a certain distance from the specimen's center. As discussed earlier, the fracture location is likely to occur at the points with the highest von-Mises stress and PEEQ. Moreover, a 'cap-like' shape with significant plasticity was observed in all specimens, indicating a ductile-dominated fracture mode. Surface roughness, microstructural anisotropy, or oxide layers can also lead to incomplete fracture, leaving the 'cap-shaped' feature in the specimen [33]. In contrast, the FE simulations assume an idealized geometry with perfectly uniform thickness,

homogeneous material properties, no uneven distribution of microstructural defects, and symmetric loading conditions. As a result, the cap-shaped fracture was not reproduced in the simulations, instead, a uniform circumferential fracture was predicted.

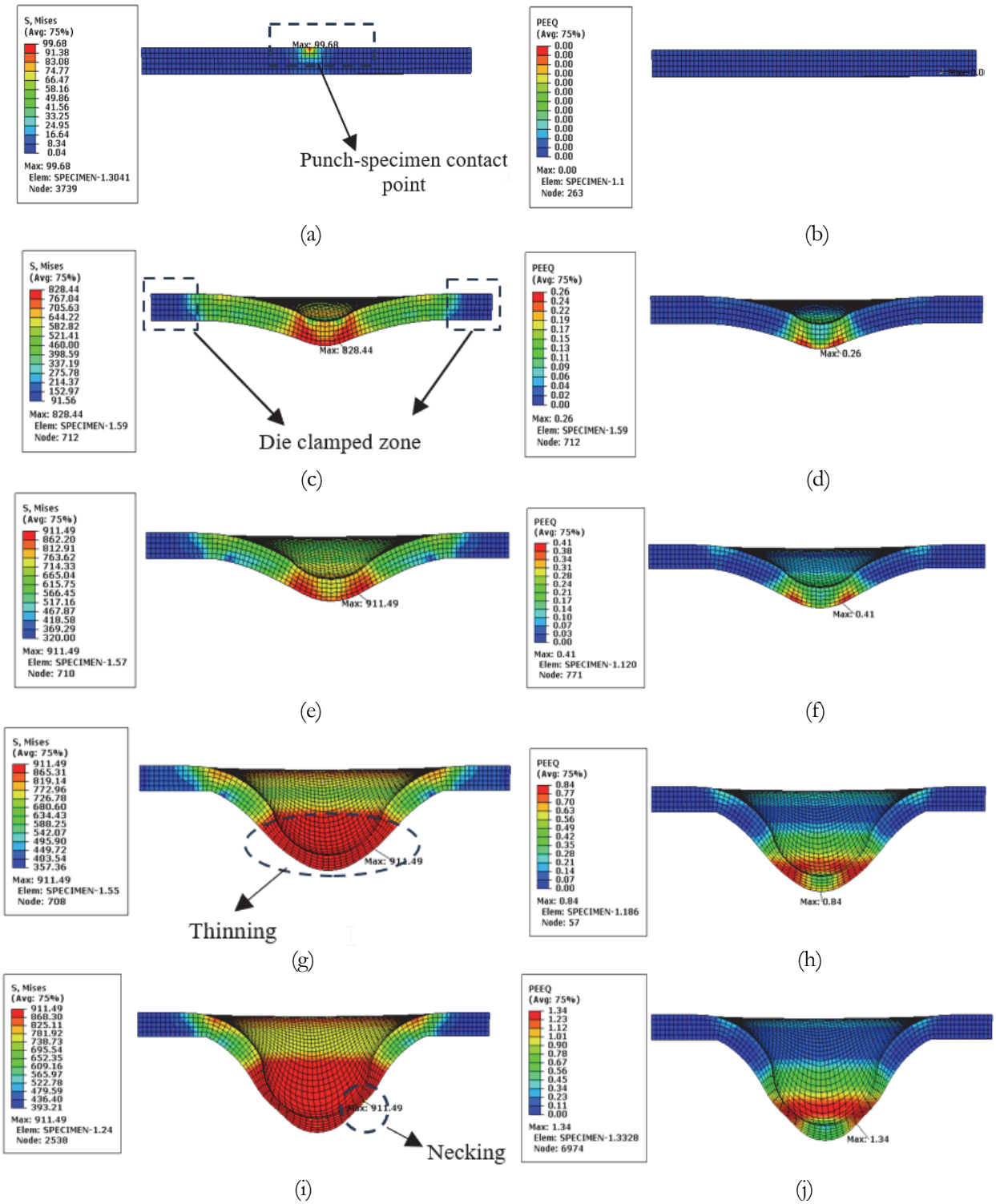

Figure 15: von-Mises stress and plastic strain distribution contours of as-received specimen at different zones: (a-b) elastic, (c-d) plastic, (e-f) membrane stretching, (g-h) tensile instability and (i-j) fracture.

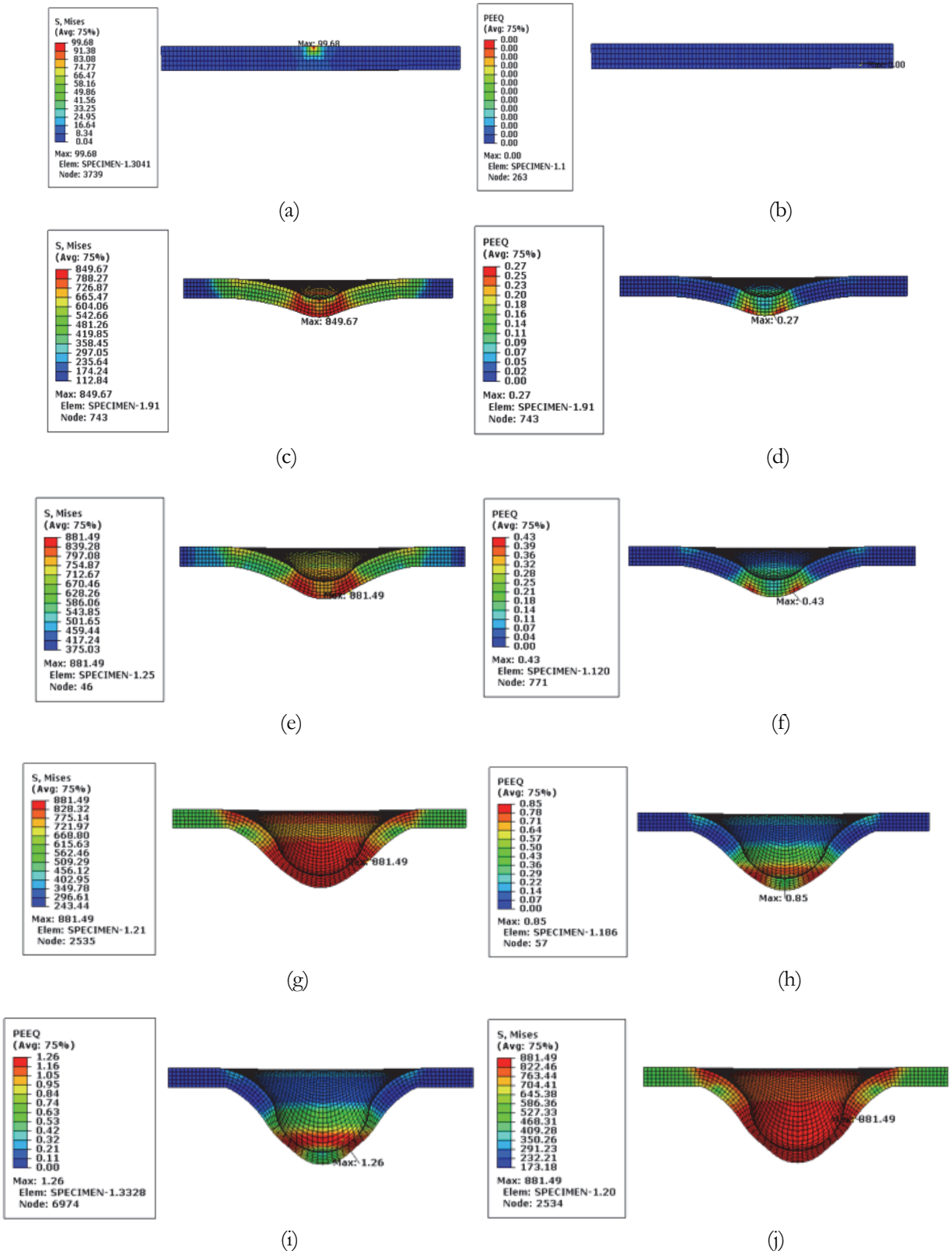

Figure 16: von-Mises stress and plastic strain distribution contours of 12% pre-strained specimen at different zones: (a-b) elastic, (c-d) plastic, (e-f) membrane stretching, (g-h) tensile instability and (i-j) fracture.

Besides, the specimen also experienced thinning along the contact surface between punch and specimen. Once thinning begins, the cross-sectional area decreases, increasing local stress under constant load. This accelerates plastic deformation and promotes severe strain localization, eventually leading to fracture initiation in the thinnest point. The claim is supported

by the FE image shown in Fig. 15 to Fig. 16, where the specimen experiences localized plastic deformation before fracture. Furthermore, the scanning electron microscopy (SEM) images of the half-sliced specimens are also shown in Fig. 17 to Fig. 20. These figures further confirm the occurrence of thinning and a limited degree of necking. It is worth noting that no clear damage such as voids or cavities was found in the material, neither at the thinnest thickness nor the area adjacent to the fracture surface.

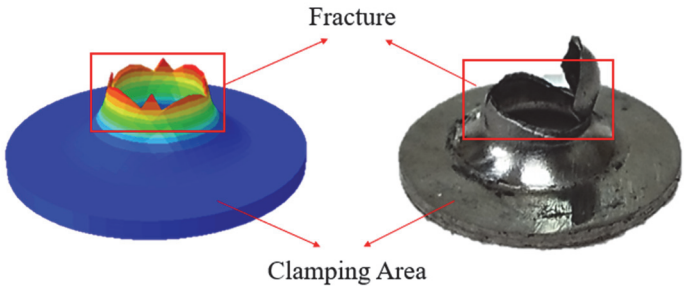

(a) (b)

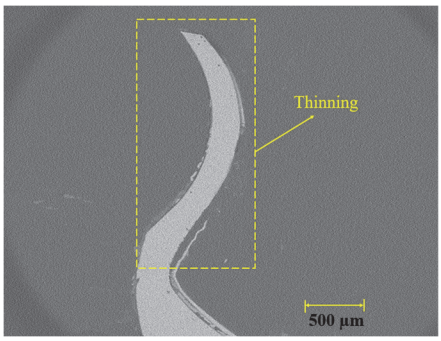

(c)

Figure 17: Fracture of as-received specimen: (a) FE simulation, (b) SPT and (c) half-sliced specimen under SEM.

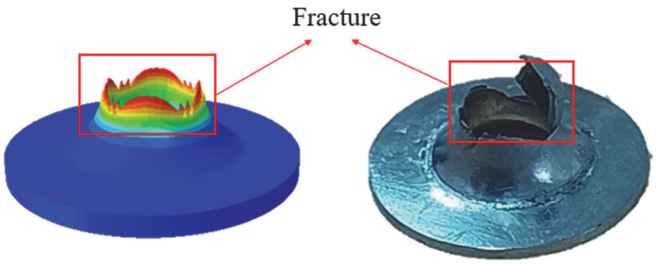

(a) (b)

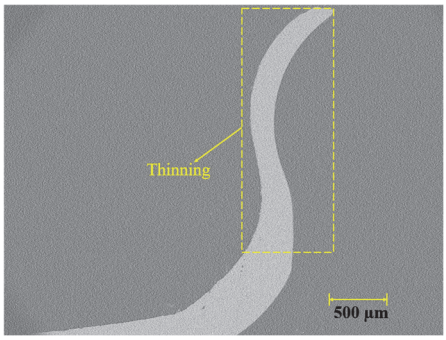

(c)

Figure 18: Fracture of 4% pre-strained specimen: (a) FE simulation, (b) SPT and (c) half-sliced specimen under SEM.

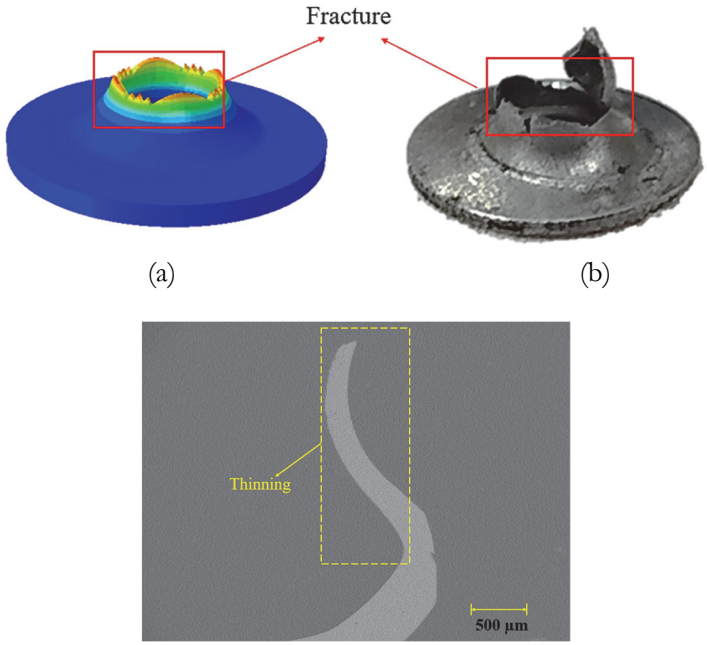

Figure 19: Fracture of 8% pre-strained specimen: (a) FE simulation, (b) SPT and (c) half-sliced specimen under SEM.

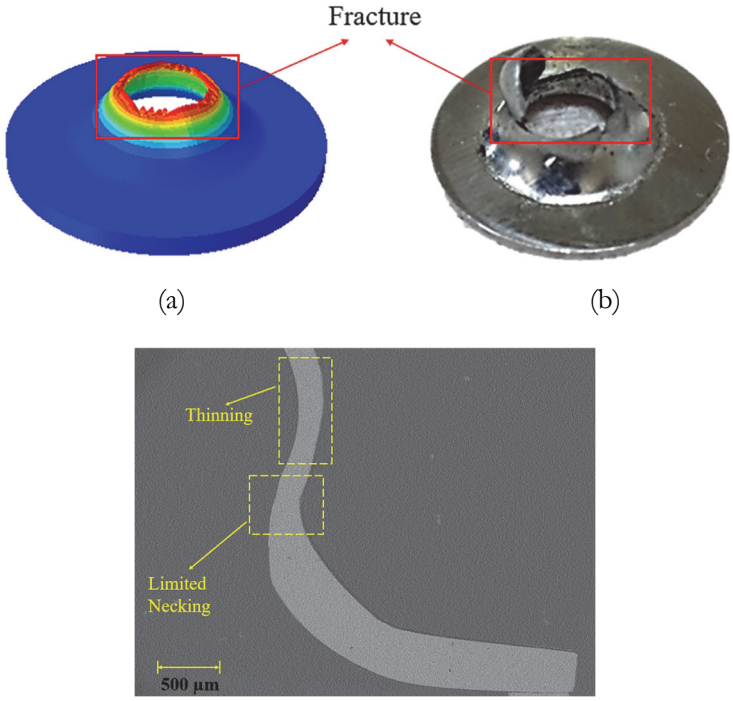

Figure 20: Fracture of 12% pre-strained specimen: (a) FE simulation, (b) SPT and (c) half-sliced specimen under SEM.

The microscopic examination was performed on the fractured specimen to further investigate the fracture behaviour of the pre-strained material under small punch load. Generally, each specimen with different pre-strain levels showed distinct fracture behaviour. Based on the examination, the as-received Grade 91 steel reveals predominantly ductile failure features as shown in Fig. 21. The fracture surfaces exhibit uniformly distributed dimples, which result from microvoid nucleation, growth, and coalescence, indicating typical ductile fracture characteristics. In Grade 91 steel, such microvoids predominantly initiate at interfaces associated with carbide particles, particularly $M_{23}C_6$ along prior austenite grain and lath boundaries, and MX carbonitrides within the martensitic lath matrix, which act as stress concentration sites during deformation [25]. These

dimples vary slightly in size and depth, which suggests significant plastic deformation occurred prior to fracture. Furthermore, there is no evidence of flat fracture surfaces, cracks, or cleavage facets, confirming the absence of brittle failure. This implies that the as-received Grade 91 steel exhibits high ductility.

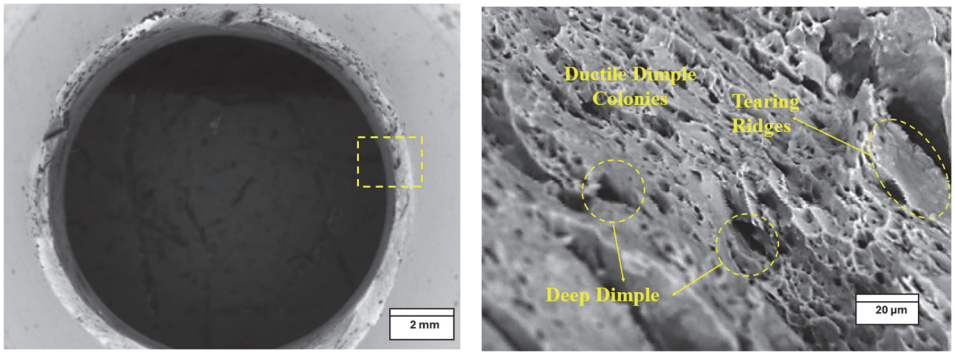

(a) (b)

Figure 21: Fractographic examination of the fracture surface of as-received specimen.

Fig. 22 shows the SEM image of fracture surface for the 4% pre-strained specimen. Detailed observation reveals slightly different features, indicating reduced ductility compared to the as-received specimen. Smaller dimples are evident, suggesting that pre-straining leads to strain hardening and restricted plastic deformation. Moreover, the dimples appear more elongated, probably due to the prior stretching during pre-straining. The fracture surfaces appear smoother, with less evidence of ductile tearing. This implies a relatively cleaner fracture surface with reduced plasticity before failure. The stretched microvoids and elongated dimples highlight the material's transition toward a less ductile failure mode, attributed to the pre-straining process. Pre-strain forces dislocations to move and pile up at prior austenite grain boundaries (PAGBs) and martensitic lath boundaries. These pile-ups create intense local stress concentrations that are high enough to nucleate a cleavage crack or decohere a grain boundary, before the surrounding matrix can redistribute stress by further plastic flow [34].

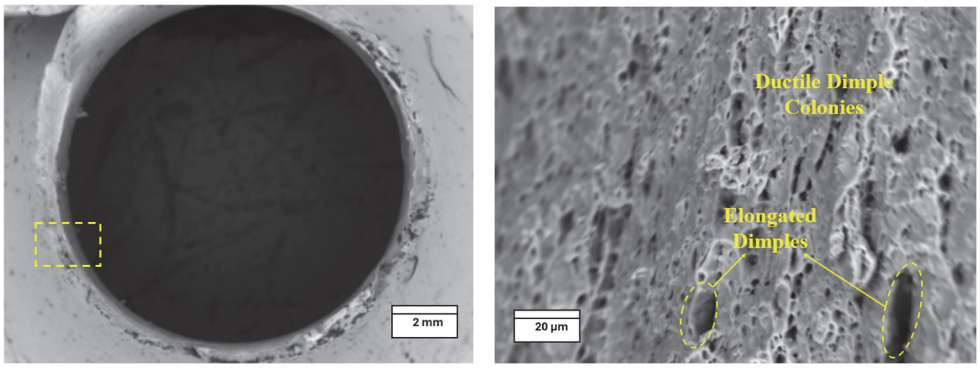

(a) (b)

Figure 22: Fractographic examination of the fracture surface of 4% pre-strained specimen.

Fig. 23 shows the fractography of the 8% pre-strained specimen. The SEM image reveals similar fracture surfaces characteristics to those of the 4% pre-strained specimen. However, the 8% pre-strained specimen contains relatively smaller dimples compared to the 4% pre-strained specimen. Additionally, the fracture surface is comparatively smoother. Quasi-cleavage features are also evident, which are indicative of a ductile-to-brittle transition mechanism [32]. Overall, these observations suggest that the 8% pre-strained specimen is less ductile compared to the as-received and 4% pre-strained specimens.

Fig. 24 shows the fractography image of the 12% plastically pre-strained specimen. It is clearly observed that the fracture surface exhibits facets and flats regions, indicative of transgranular cleavage fracture. This suggests that brittle fractures mechanisms begin to dominate, with materials experiencing minimal plastic deformation prior to failure. Unlike ductile materials, the fracture surfaces of 12% pre-strained specimens show a lack of dimples and microvoid coalescence. This is due to the pre-strain consumes the readily available mobile dislocation sources. When subsequent loading is applied, there are fewer fresh dislocations available to deform material plastically [35]. Overall, the observed fracture features suggest that

pre-straining has significantly reduced the material's ability to undergo plastic deformation, thereby increasing its susceptibility to brittle failure.

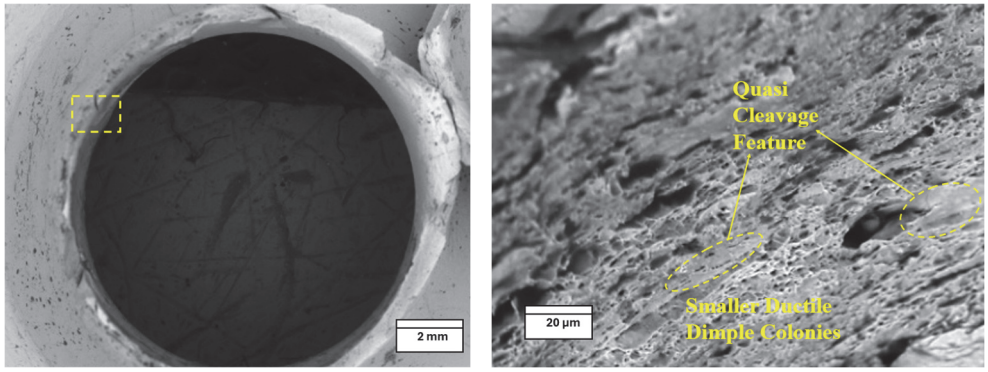

(a) (b)

Figure 23: Fractographic examination of the fracture surface of 8% pre-strained specimen

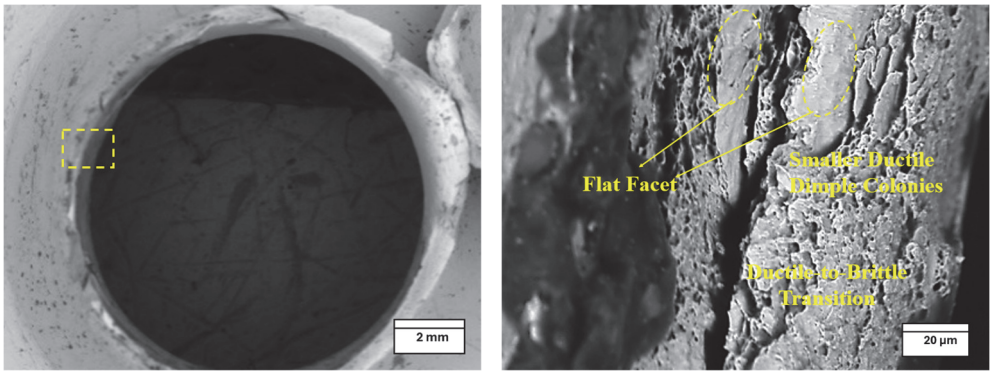

(a) (b)

Figure 24: Fractographic examination of the fracture surface of 12% pre-strained specimen.

CONCLUSION

This paper investigates the deformation and fracture behaviour of pre-strained Grade 91 steel both using both experimental and FE modelling approaches. Based on the findings, the following conclusions can be drawn.

I. Pre-straining significantly alters the load–displacement response of Grade 91 steel. The yield load increases with increasing plastic pre-straining. When comparing the as-received and 12% pre-strained materials, the yield load increased by approximately 83%, indicating a significant increase in yield strength. Conversely, the maximum load gradually decreases as the pre-straining level increases. Furthermore, the punch displacement at maximum load is also influenced by pre-straining. Although some fluctuations are observed, the displacement at maximum load generally decreases with increasing pre-strained level.

II. At low pre-strain level, the material exhibited ductile fracture behaviour. Fracture process initiates with thinning and subsequently progresses to necking. However, for 12% pre-strained material, a mixed ductile-to-brittle fracture mode is observed. As the pre-strain level increases, the ductile dimples gradually reduce in size and eventually disappear, being replaced by flatter fracture surfaces. This clearly indicates a reduction in ductility with increasing pre-straining.

III. The finite element model accurately reproduces the load–displacement response of Grade 91 steel in the small punch test across all deformation stages, confirming the reliability of the modelling framework. Among the methods, the Mao and t/100 methods provide the most accurate and consistent yield load predictions for all pre-strain levels, whereas the t/10 method systematically overpredicts the yield load. The CEN method shows reasonable agreement but deviates at low pre-strain, likely due to overestimation of strain hardening. This tendency is also reflected in the plastic bending and membrane stretching stages, where simulated loads are slightly higher

than experimental values. For the maximum load, FE predictions agree well with experiments, with errors below 10% for all cases. The best agreement is obtained at 4% pre-strain (0.5% error), while the largest deviation at 8% pre-strain (5.94%) is attributed to uncertainties in the strain-hardening input.

The findings reported in this paper helps engineers to assess in-service Grade 91 components under the influence of plasticity at localized regions. Since the validated FE model developed in this study can interpret the test result in terms of deformation and fracture behaviour under pre-strained effect, it is a practical tool for deciding whether a component that has been in service and accumulated plastic strain, is still safe to operate. Furthermore, the FE model can be used to conduct parametric studies which are time-consuming and difficult to achieve experimentally. For future work, the existing small punch test setup can be extended to include elevated temperature conditions, so that the combined effects of temperature and pre-straining can be investigated. This would better represent the actual service environment of pre-strained Grade P91 steel. Such an approach would enable the development of temperature-dependent correction factors within the correlation constants, thereby enhancing the predictive capability of the models.

ACKOWLEDGEMENT

The authors would like to express gratitude to Universiti Malaysia Pahang Al-Sultan Abdullah (UMPSA) for funding this research under the International Publication Grant RDU253304.

DECLARATION OF COMPETING INTEREST

The authors declare no conflicts of interest. There are no known competing financial interests or personal relationships that could have appeared to influence the work reported in this paper. This paper has not been published before, is not currently being reviewed by any other journal, and will not be sent anywhere else until this journal decides.

CREDIT AUTHORSHIP CONTRIBUTION STATEMENT

S. C. Pandit: Conceptualization, Resources, Methodology, Writing - Original Draft.
N. A. Alang: Supervision, Project Administration, Funding Acquisition, Writing - Review & Editing.
J. Alias: Project Administration, Writing - Review & Editing.
M. F. Hassan: Supervision, Writing - Review & Editing.
A. H. Ahmad: Writing - Review & Editing.
M. S. Shaari: Data Curation, Formal Analysis, Writing - Review & Editing.
L. Zhao: Writing - Review & Editing.

NOMENCLATURE

Abbreviations

ASTM	American Society for Testing and Materials
SPT	Small Punch Test
UTS	Ultimate Tensile Strength
YS	Yield Strength
DBTT	Ductile-to-Brittle Transition Temperature
SEM	Scanning electron microscopy
EDX	Energy-Dispersive X-ray spectroscopy
OM	Optical Microscope
UTM	Universal Testing Machine

Symbols

E	Young's modulus
σ	Stress
σ_e	Engineering Stress
σ_t	True Stress
σ_{ys}	Yield Strength
σ_{uts}	Ultimate Tensile Strength
ε	Strain
ε_e	Engineering Strain
ε_t	True Strain

FE	Finite Element
LVDT	Linear Variable Differential Transformer
EDM	Electric Discharge Machining
HE	Hydrogen embrittlement

K	Strength coefficient
n	Strain hardening exponent.
P_y	Yield Load
P_{max}	Maximum Load
δ_m	Displacement at Maximum Load
δ_f	Displacement at Fracture
a_1, a_2	Yield Strength Correlation Constant
β_1, β_2	Ultimate Tensile Strength Correlation Constant
t	Thickness of the specimen
d	Diameter of the Punch
μ	Coefficient of Friction

REFERENCES

[1] Jin, X., Wang, R.-Z., Shu, Y., Fei, J.-W., Wen, J.-F., Tu, S.-T. (2021). Creep-Fatigue Crack Initiation Simulation of a Modified 12% Cr Steel Based on Grain Boundary Cavitation and Plastic Slip Accumulation, Materials (Basel), 14(21), pp. 6565, DOI: https://doi.org/10.3390/ma14216565.

[2] Nguyen, T.T., Yoon, K.B., Park, J., Baek, U.B. (2022). Characterization of Strain-Controlled Low-Cycle fatigue and fracture behavior of P91 steel at elevated temperatures, Eng. Fail. Anal., 133, pp. 105887, DOI: https://doi.org/10.1016/j.engfailanal.2021.105887.

[3] Zhao, L., Song, Y., Xu, L., Han, Y., Hao, K. (2024). Investigation of the High-Temperature Low-Cycle fatigue failure characteristics of P91 steel weld joints and their fatigue strength reduction factors under various load control regimes, Int. J. Fatigue, 180, pp. 108085, DOI: https://doi.org/10.1016/j.ijfatigue.2023.108085.

[4] Abebe, B.A., Altuncu, E. (2024). A Review on hydrogen embrittlement behavior of steel structures and measurement methods, Int. Adv. Res. Eng. J., 8(2), pp. 91–101, DOI: https://doi.org/10.35860/iarej.1414085.

[5] Junak, G., Adamiec, J., Łyczkowska, K. (2024). Mechanical Properties of P91 Steel (X10CrMoVNb9-1) during Simulated Operation in a Hydrogen-Containing Environment, Materials (Basel)., 17(17), pp. 4398, DOI: https://doi.org/10.3390/ma17174398.

[6] Sun, X., Che, C., Qian, G., Wang, X. (2024). Microstructure, hardness and creep properties for P91 steel after long-term service in a ultra-supercritical power plant, Int. J. Press. Vessel. Pip., 212, pp. 105330, DOI: https://doi.org/10.1016/j.ijpvp.2024.105330.

[7] Gülçimen Çakan, B., Soyarslan, C., Bargmann, S., Hähner, P. (2017). Experimental and Computational Study of Ductile Fracture in Small Punch Tests, Materials (Basel)., 10(10), pp. 1185, DOI: https://doi.org/10.3390/ma10101185.

[8] Torres, J., Gordon, A.P. (2021). Mechanics of the small punch test: a review and qualification of additive manufacturing materials, J. Mater. Sci. , 56(18), pp. 10707–44, DOI: https://doi.org/10.1007/S10853-021-05929-8.

[9] Arunkumar, S. (2020). Overview of Small Punch Test, Met. Mater. Int., 26(6), pp. 719–738, DOI: https://doi.org/10.1007/S12540-019-00454-5.

[10] Cuesta, I.I., Alegre, J.M. (2012). Hardening evaluation of stamped aluminium alloy components using the Small Punch Test, Eng. Fail. Anal., 26, pp. 240–6, DOI: https://doi.org/10.1016/j.engfailanal.2012.06.004.

[11] Shu, H., Zhang, J., Yang, S., Ling, X., Peng, H. (2024). Small punch evaluation of mechanical properties for 310S stainless steel considering pre-strain effect, Int. J. Press. Vessel. Pip., 210, DOI: https://doi.org/10.1016/j.ijpvp.2024.105236.

[12] Peng, J., Li, K., Dai, Q., Gao, G., Zhang, Y., Cao, W. (2019). Estimation of mechanical strength for pre-strained 316L austenitic stainless steel by small punch test, Vacuum, 160, pp. 37–53, DOI: https://doi.org/10.1016/j.vacuum.2018.11.015.

[13] Calaf-Chica, J., Sánchez Palomar, M., Bravo Díez, P.M., Preciado Calzada, M. (2021). Deviations in yield and ultimate tensile strength estimation with the Small Punch Test: Numerical analysis of pre-straining and Bauschinger effect influence, Mech. Mater., 153, DOI: https://doi.org/10.1016/j.mechmat.2020.103696.

[14] Lucon, E., Benzing, J.T., Derimow, N., Hrabe, N. (2021). Small Punch Testing to Estimate the Tensile and Fracture Properties of Additively Manufactured Ti-6Al-4V, J. Mater. Eng. Performance(JMEP), 30(7), pp. 5039–5049, DOI: https://doi.org/10.1007/S11665-021-05603-9.

[15] Chen, H., Yang, R., Al-Abedy, H.K., Li, H., Sun, W., Jones, I.A. (2020). Characterisation of deformation process and fracture mechanisms of P91 steel at 600 °C in small punch tensile testing, Mater. Charact., 168,

DOI: https://doi.org/10.1016/j.matchar.2020.110514.
[16] Woo, W., Jeong, J.S., Kim, D.-K., Lee, C.M., Choi, S.-H., Suh, J.-Y., Lee, S.Y., Harjo, S., Kawasaki, T. (2020). Stacking Fault Energy Analyses of Additively Manufactured Stainless Steel 316L and CrCoNi Medium Entropy Alloy Using In Situ Neutron Diffraction, Sci. Rep., 10(1), pp. 1350, DOI: https://doi.org/10.1038/s41598-020-58273-3.
[17] Ferdous, I.U., Alang, N.A., Alias, J., Nadzir, S.M. (2021). Numerical Prediction of Creep Rupture Life of Ex-Service and As-Received Grade 91 Steel at 873 K, Int. J. Automot. Mech. Eng., 18(3), pp. 8845–8858, DOI: https://doi.org/10.15282/ijame.18.3.2021.01.0678.
[18] Oliveira, D.M., San Marchi, C.W., Medlin, D.L., Gibeling, J.C. (2025). Hydrogen influences thermal activation parameters for dislocation glide during low cycle fatigue of 316L stainless steel, Mater. Sci. Eng. A, 932, pp. 148243, DOI: https://doi.org/10.1016/j.msea.2025.148243.
[19] Cheng, Z., Sun, J., Tai, P., Zhang, L., Wei, Y., Chang, H., Thuku, R., Gichuhi, K.M. (2021). Comparative Study between Small Punch Tests and Finite Element Analysis of Miniature Steel Specimens, J. Mater. Eng. Perform., 30(12), pp. 9094–9107, DOI: https://doi.org/10.1007/S11665-021-06098-0.
[20] ASTM International. (2024). Standard test methods for tension testing of metallic materials (ASTM E8/E8M-24). DOI: https://doi.org/10.1520/E0008_E0008M-24
[21] ASTM International. (2020). Standard test method for small punch testing of metallic materials (ASTM E3205-20). DOI: https://doi.org/10.1520/E3205-20
[22] Ul Ferdous, I., Alang, N.A., Alias, J., Ab Razak, N., Abu Samah, Z. (2022). Evaluation of Yield Strength Under Small Punch Loading with Different Specimen Thicknesses, J. Adv. Res. Appl. Sci. Eng. Technol., DOI: https://doi.org/10.37934/cfdl.XX.X.XX.
[23] García, T.E., Rodríguez, C., Belzunce, F.J., Suárez, C. (2014). Estimation of the mechanical properties of metallic materials by means of the small punch test, J. Alloys Compd., 582, pp. 708–717, DOI: https://doi.org/10.1016/j.jallcom.2013.08.009.
[24] Moreno, M.F. (2018). Effects of thickness specimen on the evaluation of relationship between tensile properties and small punch testing parameters in metallic materials, Mater. Des., 157, pp. 512–522, DOI: https://doi.org/10.1016/j.matdes.2018.07.065.
[25] Peng, J., Vijayanand, V.D., Knowles, D., Truman, C., Mostafavi, M. (2021). The sensitivity ranking of ductile material mechanical properties, geometrical factors, friction coefficients and damage parameters for small punch test, Int. J. Press. Vessel. Pip., 193, pp. 104468, DOI: https://doi.org/10.1016/j.ijpvp.2021.104468.
[26] Çakan, B.G., Soyarslan, C., Bargmann, S., Hähner, P. (2017). Experimental and Computational Study of Ductile Fracture in Small Punch Tests, Mater. , 10(10), pp. 1185, DOI: https://doi.org/10.3390/MA10101185.
[27] Pandey, C., Mahapatra, M.M., Kumar, P., Saini, N. (2018). Some studies on P91 steel and their weldments, J. Alloys Compd., 743, pp. 332–364, DOI: https://doi.org/10.1016/J.JALLCOM.2018.01.120.
[28] Li, H., Chen, H., Al-Abedy, H.K., Sun, W. (2020). Study on the Fracture Mechanism of the P91 Steel During Small Punch Tensile Testing, , pp. 106–111, DOI: https://doi.org/10.1007/978-3-030-47883-4_19.
[29] Nowik, K., Oksiuta, Z. (2022). Experimental and Numerical Small Punch Tests of the 14Cr ODS Ferritic Steel, Acta Mech. Autom., 16(3), pp. 225–232, DOI: https://doi.org/10.2478/ama-2022-0027.
[30] Li, Q., Wang, X., Zhao, L., Xu, L., Han, Y. (2023). Validation and improvement in metallic material tensile models for small punch tests, J. Mater. Sci., 58(26), pp. 10832–10852, DOI: https://doi.org/10.1007/s10853-023-08695-x.
[31] Pandit, S.C., Alang, N.A., Ferdous, I.U., Alias, J.B., Hassan, M.F. Bin., Ahmad, A.H. Bin. (2025). Evaluation of thinning behaviour under the influence of plastic hardening and surface friction during small punch test, Fract. Struct. Integr., 19(72), pp. 46–61, DOI: https://doi.org/10.3221/IGF-ESIS.72.05.
[32] Alang, N.A., Ferdous, I.U., Alias, J., Razak, N.A.A., Ahmad, A.H. (2024). On the Influence of Clamping Force and Contact Friction in Small Punch Test, Lect. Notes Mech. Eng., , pp. 175–182, DOI: https://doi.org/10.1007/978-981-97-4806-8_15.
[33] Shaik, A.R., Pandey, A.V., Karthik, V., Kolhatkar, A., Abhishek, G., Divakar, R. (2024). Application of Digital Image Correlation to Small Punch Test for Determination of Stress–Strain Properties, Trans. Indian Inst. Met., 77(11), pp. 3879–3892, DOI: https://doi.org/10.1007/s12666-024-03442-5.
[34] Zhang, K., Liu, X., Fan, P., Zhu, L., Wang, K., Wang, L., Zhao, C. (2023). Characterization of geometrically necessary dislocation evolution during creep of P91 steel using electron backscatter diffraction, Mater. Charact., 195, pp. 112501, DOI: https://doi.org/10.1016/j.matchar.2022.112501.
[35] Zhang, J., Yu, Q., Tian, J., Yang, S., Zuo, X., Li, Y., Chen, N., Rong, Y., Ritchie, R.O., Lu, J. (2025). Toughness enhancement by massive dislocation absorption at the crack front, Proc. Natl. Acad. Sci., 122(37), DOI: https://doi.org/10.1073/pnas.2511830122.